

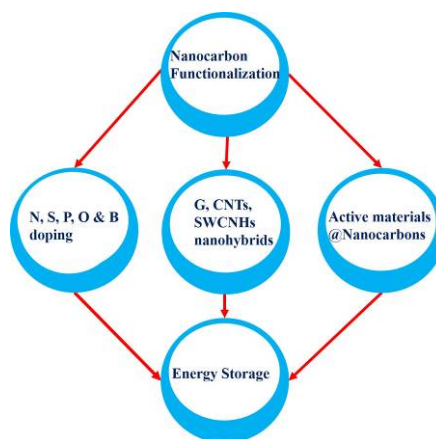
# Accounts of Materials & Surface Research

## A Mini-Review on Functionalized Porous Nanocarbons for the Applications in Electro-Chemical Energy Storage

K. P. Annamalai and Yousheng Tao\*

CAS Key Laboratory of Design and Assembly of Functional Nanostructures, Haixi Institutes, Chinese Academy of Sciences (CAS), Fujian 350002, China  
taoys@tom.com

Nanocarbons offer large surface to volume ratio, favorable mass and charge transfer, excellent chemical stability and exceptional electro-chemical properties, which have inspired the utilization of the materials in energy storage. In order to enhance their performance researchers have focused on developing functionalized porous nanocarbons. The approaches are known as incorporating heteroatoms or combining with active materials *via* chemical surface modification, physical mixing and in-situ formation. Continuous efforts have been undertaken to fabricate nanocarbon hybrids because of the synergistic effect of their individual components. This article briefly reviewed the recent progress and development in functionalization of porous nanocarbons and their advantages in enhancing the performance in electro-chemical energy storage.



**Keyword:** nanocarbons, carbon nanotubes, single wall carbon nanohorns, graphene, nanopores, functionalizations, applications, energy storage, capacitance

**K. P. Annamalai** received his M.Sc from National Institute of Technology, India (2010) and the Ph.D. degree from the University of Chinese Academy of Sciences, China (2015). He presently works as post-doc fellow hosted by Prof. Y. Tao in CAS Haixi Institutes, China. Dr. Annamalai currently focuses on nanocarbons and their supported metal component nanostructures for energy storage/conversion and environment protection.



**Yousheng Tao** received a PhD in Chemistry in 2004 from Chiba University, Japan, and a PhD in Geological Science in 2006 from the Chinese Academy of Geological Science, China. Since he joined the ICST of Shinshu University in 2008, he has been working on nanoporous carbons, mesoporous zeolites, nanosolutions and development of environmental protection techniques. Earlier, he worked as an Associate Professor and a Senior Engineer in the Environmental Science Research Center, Xiamen University, China, and as a postdoctoral and JSPS Researcher in Chiba University, Japan. Now he is a Professor in CAS Haixi Institutes, also a guest professor in Sichuan University, China and the Editor-in-Chief of Recent Innovations in Chemical Engineering.



# A Mini-Review on Functionalized Porous Nanocarbons for the Applications in Electro-Chemical Energy Storage

K. P. Annamalai and Yousheng Tao\*

CAS Key Laboratory of Design and Assembly of Functional Nanostructures, Haixi Institutes, Chinese Academy of Sciences (CAS), Fuzhou, Fujian 350002, China  
[taoys@tom.com](mailto:taoys@tom.com)

## 1. Introduction

Nanometer-sized materials always differ from the micro- or bulk-sized materials and their properties offer possibilities for widen their applications in versatile fields. Dimensionally confined  $sp^2$  bonded carbon analogues such as carbon nanotubes (CNTs), single wall carbon nanohorns (SWCNHs) and graphene (G) were the typical nanocarbons. Their unique nanostructures lead to unprecedented intrinsic properties, which triggered to intensive exploration in basic as well as applied researches. Potential applications of the nanocarbons are huge including gas storage/separation, transparent conductive thin films, photo detectors, sensors and energy storage applications including supercapacitor, Li-batteries and fuel cells [1]. These potential applications are strongly relied on their large surface area, high chemical stability, unique mass and charge transfer.

In particular, nanocarbons demonstrate to be an excellent candidate for energy storage materials [2]. Tremendous progress has been made in investigating nanocarbons for enhanced energy storage; some technologies have been developed and commercialized. The performance of nanocarbon materials can be further improved by incorporating heteroatoms or combining with active materials *via* (i)

chemical surface modification, (ii) physical mixing and (iii) in-situ formation. Many nanocarbon hybrids display enhanced performance or even exhibit new properties because of the synergistic effect of their individual components. Several excellent review articles and books were published dealing with fundamentals and technical pathway to design and characterize their nano-structures [3]. This article briefly reviewed the recent progress in the development of functional nanocarbons and hybrids and their potential applications in electro-chemical energy storage.

## 2. Functionalization of nanocarbons

There are plenty of methods to prepare functionalized nanocarbons, their hybrids and active material loaded ones. The functionalization strategies mainly come under the categories of covalent reaction, non-covalent interaction, electrostatic interaction and electrochemical deposition.

### 2.1 CNTs, SWCNHs and Graphene with heteroatom-doping

The formation of heteroatom-doped nanocarbon structures can be realized through two different routes: "in situ" doping (chemical vapor deposition, arc-discharge approaches, etc.) and post-synthesis

treatment such as thermal treatment with heteroatom precursors. The former allows for the direct incorporation of dopant elements into the carbon lattice during the growth process, while the latter mainly refers to the post-treatment of nanocarbons with the heteroatom-containing precursors. Doping tunes the electronic properties of carbon materials due to the perturbation of the electron distribution of their  $sp^2$ -hybridized and conjugated graphitic structure by the dopant atoms of different electronegativity. The dopant atoms lead to the charge delocalization, density of donor states near Fermi level, conductivity and electron-transfer rates of nanocarbon materials relatively higher than the un-doped ones. It makes the materials highly active for many applications [4]. Tremendous efforts have been made towards the preparation of carbon materials, especially hierarchical porous nanostructures, with single or multiple heteroatom doping to achieve enhanced performance.

Recently, Murakoshi et al. [5] reported a Fe-N-doped vertical CNTs via simple mixing of vertically aligned CNTs (VA-CNTs) and iron phthalocyanine (FePc). Due to their strong affinity through  $\pi$ - $\pi$  interaction, FePc converted into catalytically active Fe-N-C structures on the VA-CNTs through pyrolysis (Figure 1a). TEM image revealed that almost all of the VA-CNT surfaces were coated homogeneously with the graphene-like moieties with the thickness of one to few layers (Figure 1b). The nano-sized graphene-like materials wrapped around the VA-CNTs during pyrolysis of the FePc. The materials had  $\sim$  40%,  $\sim$  20% and  $\sim$  30% of pyridinic, pyr-

rolic and quaternary N species. Since the pyridinic N species have a lone pair of electrons and are able to coordinate various metal ions, they play a significant role in Fe-N-C active site formation.

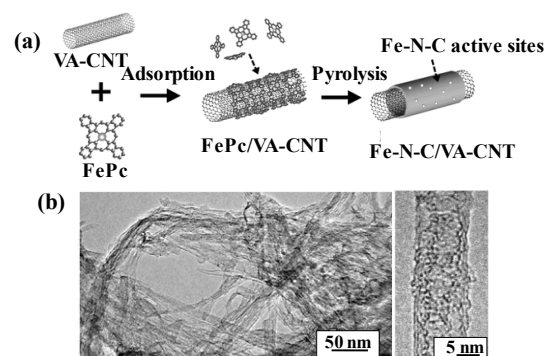


Figure 1. (a) Scheme for adsorption of iron(II) phthalocyanine (FePc) on a VA-CNT to yield an FePc/VA-CNT composite and subsequent pyrolysis to yield the Fe-N-C/VA-CNT catalyst and (b) TEM and HR-TEM images of as-grown Fe-N-VA-CNT. Reprinted from ref. 5. Copyright 2015 WILEY-VCH Verlag GmbH & Co. KGaA, Weinheim.

To enhance the performance of doped CNTs, Qiao et al. [6] investigated a route to synthesis co-doped (i.e. nitrogen and sulfur) CNTs using polydopamine (PDA) precursors. The oxidized CNTs were mixed with dopamine in phosphate buffered saline (PBS) to form CNTs-PDA hybrid. 2-mercaptoethanol was used to modify the PDA group. Further pyrolysis produced nitrogen and sulfur doped CNTs. TEM image shown in Figure 2 clarified the coating of PDA-derived carbon on CNT surface. Elemental mapping images assured the uniform distribution of N, S and O. As shown in Raman spectra (Figure 2g),  $I_d/I_g$  ratio of N,S-CNTs (0.78) higher than that of N-CNTs (0.71) illustrated that sulfur incorporation caused defects and disordered

structures. Although the electronegativity of S (2.58) and C (2.55) are nearly identical, the co-doped samples showed higher activity than single doped materials. It might be attributed to the spin density correlation, which was significantly higher in co-doped models than the N alone doped CNTs. Hence larger number of carbon atoms could serve as electroactive sites to absorb  $H^*$  and  $OOH^*$  species after the secondary element doping. As a result, the co-doped CNTs had significantly higher activities of hydrogen evolution reaction (HER) and oxygen evolution reaction (OER) than the single doped ones.

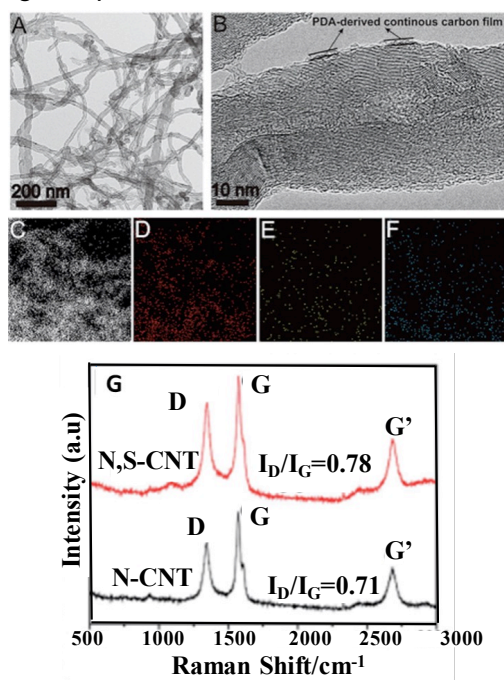


Figure 2. (A) TEM and (B) the magnified TEM images of the N,S-CNT, (C–F) TEM elemental mapping of C, O, N, and S in N,S-CN, (G) Raman spectra of N-CNT and N,S-CNT. Reprinted from ref. 6. Copyright 2016 WILEY-VCH Verlag GmbH & Co. KGaA, Weinheim.

Similarly to demonstrate the effect of co-doping on graphene, Huang et al. followed the two-step method: (1) adsorp-

tion and coverage of 1,3,4-thiadiazole-2,5-dithiol (TDDT) on the graphene oxide (GO) *via* a hydrothermal process; (2) incorporation of N and S atoms into the carbon network by thermal annealing under Ar. N and S doped G (NS-Gs) not only created abundant reactive regions for various catalytic reactions, but also provided a large number of accessible sites for binding metal or metal oxide nanoparticles. The typical SEM and TEM images (Figure 3a-c) revealed that the thin and transparent NS-Gs remained separately from each other, suggesting that their 2D nature was well preserved during the doping process. The co-existence of C, N, and S components was evidenced with the element mappings (Figure 4d-g). The pyridinic N and pyrrolic N as well as thiophene S atoms doped nanosheets were used as excellent platform for the uniform distribution of Pt particles with an average diameter of 2.5 nm [7].

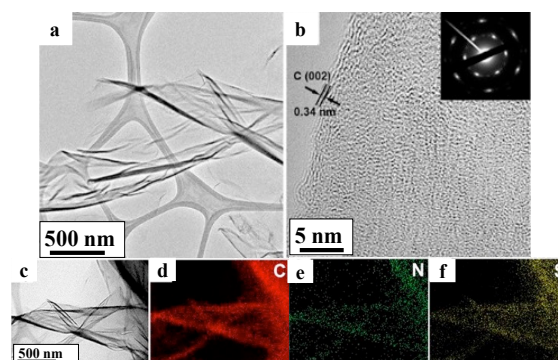


Figure 3. (a) TEM, (b) HRTEM, (c) scanning transmission electron microscopy (STEM) images of the NS-G sheets and corresponding elemental mapping of (d) carbon, (e) nitrogen and (f) sulfur. Inset in (b): SAED pattern of NS-G. Reprinted from ref. 7. Copyright 2016 American Chemical Society.

Ito et al. [8] investigated the nitrogen,

phosphorus and sulfur doped nanoporous graphene via CVD method, using benzene, pyridine, thiophene and/or triphenylphosphine as carbon, nitrogen, sulfur and phosphorus precursors, respectively. Under a mixed atmosphere of argon and hydrogen, 7-8 nm NiO nanoparticles on a Cu sheet reduced to ultrafine nanoporous Ni. Such resulting 3D open porous structures and active Ni internal surfaces acted as a template and a catalyst for graphene growth. Finally, the Ni frame was removed in an acid solution, resulting N, P, S doped graphene of an open nanoporous morphology with surface area ranging from 440 to 790 m<sup>2</sup>/g. The nanosheets were of 3-6 atomic layers.

Unlike previous studies, Yuge et al. [9] disclosed the relationship between the structural variation and the doping content using SWCNHs. Nitrogen and boron co-doped SWCNHs (BN-SWCNHs) were prepared with boron containing carbon target under nitrogen atmospheres [10]. The prepared nanohorns were approximately in the sizes of 50 to 300 nm with boron and nitrogen content of 1.2 and 1.0 at.%, respectively. The structure of BN-SWCNHs was mainly of petal-dahlia type. As shown in Figure 4, SWCNH sheaths contained graphite-like thin sheets (GLSs). When the boron was contained in the target, graphene sheets preferentially formed. Whereas, the formation of graphene was especially promoted by using a boron-containing carbon target under argon atmosphere. Structural imperfection was enhanced due to the heteroatom doping (Figure 4c).

Wu et al. also elucidated the effect of doping on their morphologies of SWCNHs [11].

Boron, phosphorus, nitrogen-doped and co-doped SWCNHs were produced using arc-discharge of B<sub>4</sub>C or P(Ph)<sub>3</sub> or co-containing composite carbon rods.

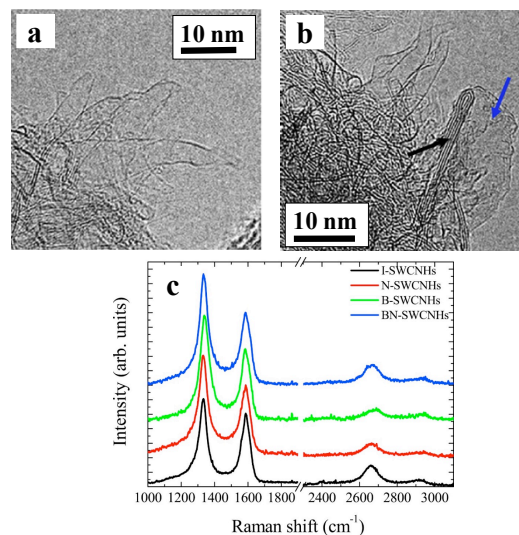


Figure 4. TEM images of (a) SWCNHs, (b) B,N-doped SWCNHs and (c) Raman spectra of l-, N-, B-, and BN-SWCNHs. Reprinted from ref. 10. Copyright 2016 Elsevier Ltd.

The bundles of SWCNHs became smaller and more isolated nanohorns occurred with the increasing content of B. As a consequence, the distorted curvature was induced by the incorporation of B atoms into the graphene lattice. Moreover, B<sub>3</sub>-SWCNHs had relatively lower I<sub>D</sub>/I<sub>G</sub> ratio and more tubular graphene carbon structures than the non-doped ones.

Wang et al. reported the relationship of structural variations of SWCNHs upon oxygen and nitrogen doping [12]. They produced the oxygen and nitrogen doped SWCNHs with typical arc discharge method with CO and NH<sub>3</sub> (3:1 ratio) precursors. HNO<sub>3</sub> treatment in room temperature for 24 h stirring triggered the doping percentage. The products achieved 9.5 wt.% N content in SWCNHs. Such doping significantly al-

tered the properties of materials such as dispersion in acid, which was verified with their wettability. As shown in Figure 5a, the wetting angle before doping is smaller ( $5^\circ$ ) than the doped SWCNHs ( $140^\circ$ ), indicating that the nitrogen and oxygen dopants considerably improved the wettability. The SWCNHs had the BET surface area of mere  $234.5 \text{ m}^2/\text{g}$ . Whereas, the N,O co-doped ones had a BET surface area of  $727.4 \text{ m}^2/\text{g}$ . The nitrogen and oxygen doping also created many mesopores in N-SWCNHs in addition to the micropores (Figure 5b).

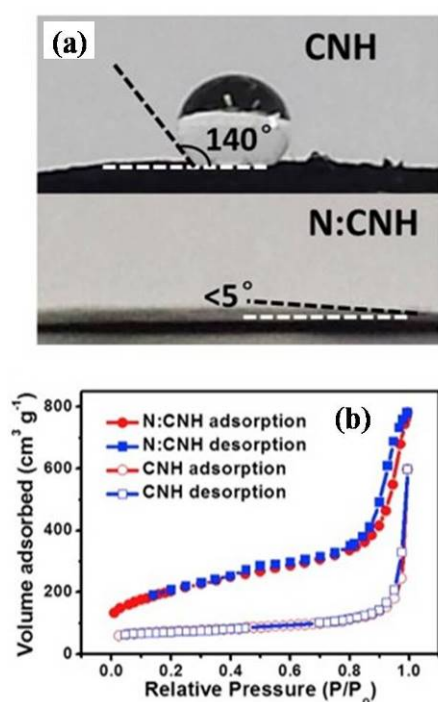


Figure 5. (a) Wetting angles of  $1 \text{ M H}_2\text{SO}_4$  droplet on the SWCNHs ( $140^\circ$ ) and N-SWCNHs ( $<5^\circ$ ) and (b) Nitrogen adsorption/desorption isotherms at 77K on SWCNHs and N-SWCNHs. Reprinted from ref. 12. Copyright 2017 Elsevier Ltd.

## 2.2 Nanocarbon hybrids

The chemical inertness, poor solubility and hydrophobicity of the nanocarbons are

challenging the hybridization process in wet chemical approach. It is a feasible hybridization technique using nanocarbon functionalization *via* covalent, noncovalent and electrostatic interaction. Pristine nanocarbons can be modified with functional groups using acids, organic linkers or ionic surfactants *via* oxidation, covalent and noncovalent functionalization [13]. The interaction between the surface-modified nanocarbons forms nanohybrid. Pristine nanocarbon as a template for the growth of second nanocarbon can also make nanohybrids. Tour et al. [14] described the electro-chemical reduction of aryl diazonium salt to functionalize the bucky paper electrode of 4-tert butyl benzene derivative CNTs. The composite showed excellent solubility in organic solvent. Yang et al. [15] stated the stable graphene suspension using water soluble hydroxypropyl cellulose or chitosan. In order to achieve SWCNHs individualization, potassium naphthalenide and some electrophiles were used to functionalize them. Such a process interestingly dismantled the SWCNHs. The individual nanohorns and successive functionalization allowed them to be soluble in DMSO solvent immediately [16]. Pagonaet al. [17] did the cone end functionalization of SWCNHs using molecular oxygen at  $580^\circ\text{C}$ , and then further converted them to acyl chloride using thionyl chloride to achieve covalent functionalization with amines, alcohols, and thiols for the generation of CNH-based amide, ester and thioester materials. Although covalent interaction achieves strongly bonded hybrid, it disrupted nanocarbon  $\pi$  networks (change in the  $\text{sp}^2\text{-sp}^3$  formation)

reduce the electronic, mechanical and thermal properties. On the contrary, non-covalent and electrostatic interaction are highly feasible with insignificant changes of nanocarbon properties. However, such hybrids often suffer from poor bounding because of weaker driving force between two nanocarbons. In order to favor the dispersion of nanocarbons in water, nanocarbons are widely modified with surfactants [13a, 18]. Actually non-covalent modification imports an electrostatic repulsive force in adjacent nanocarbons, preventing the nanocarbons from aggregation. Stable aqueous dispersion of nanocarbons are usually made with sodium dodecyl benzen sulfonate (SDBS), cetyltrimethylammonium p-toluenesulfonate (CTAT), cetyltrimethylammonium bromide (CTAB) and sodium cholate (SC) under sonication [19]. Collier et al. [20] demonstrated the SWCNTs dispersion using water soluble porphyrin components. Single stranded DNA was also able to disperse the CNTs in aqueous solution and exhibit selective affinity towards semi-conductive CNTs. Precipitation or re-dispersion occurred just by lowering the pH to 4 or raising to 7.

Oxidation of carbon using acids ( $\text{HNO}_3:\text{H}_2\text{SO}_4=1:3$ ) could provide carboxyl and hydroxyl functional groups and most of the functional groups located on the edges and tips of carbons. Such a simple procedure allows to modified the surface of nanocarbons to obtain a range of carboxyl and hydroxyl groups, which are useful for metal ions to be loaded on nanocarbons. Dai et al. [21] synthesized graphene/carbon nanotube (G/CNT) hybrids with poly(ethyleneimine) (PEI) modified

graphene nanosheets (GNs). The  $\text{NH}_2$  groups in the modified graphene were protonated ( $\text{NH}_3^+$ ) after dissolving PEI into distilled water. This positively charged graphene sheets having PEI chains (PEI-GNs) could not only render the GNs to be dispersible, but also made it possible for controllably fabricating multi-component nanohybrid films with acid functionalized CNTs. Thickness of the thin films were easily controlled by repeated self-assembly process. Chen et al. [22] prepared the G/CNT heterostructures hydrogels of high specific surface area ( $237 \text{ m}^2/\text{g}$ ) with CNTs as spacer to prevent the graphene from aggregation.

Izadi-Najafabadi mixed the SWCNT and SWCNHs with DMF under 24h sonication. The resultant dispersion was poured into the petri dish and resting at the temperature  $100^\circ\text{C}$ . Upon solvent evaporation self-supported hybrids thin film was achieved [23]. The hybrids had high conductivity and large meso-macro porosity that facilitated the ion transportation and charge transfer, giving obviously enhanced performance (such as power delivery) of the hybrids with comparison to their individual counterparts. Zheng et al. [24] prepared the G/SWCNTs by means of Langmuir-Blodgett assembly. GO and acid functionalized SWCNTs were mixed in the water/methanol mixture and assembled thin films. The obtained films were further thermally annealed at  $1100^\circ\text{C}$  to get reduced thin nanohybrids. Similarly, Ramaprabhu et al. [25] investigated G/CNT nanohybrids using different graphite precursors, i.e. solar exfoliated graphite (SEG) functionalized with the poly-electrolyte of

PDDA (0.5 wt.%). Addition of NaCl into their stable aqueous dispersion endorsed the functionalization by affecting the polymer chain configuration on poly-electrolyte. Acid functionalized MWCNTs were refluxed with concentrated  $\text{H}_2\text{SO}_4$  and  $\text{HNO}_3$  in the ratio (3:1) for 24 h at  $80^\circ\text{C}$  (Figure 6). The prepared stable SEG and MWCNTs dispersion was mixed and stirred for 12 h at room temperature to obtain nanohybrids. The conductivity of nanohybrids was higher than their individual components, which facilitated the charge transport at the interface between electrode and electrolyte.

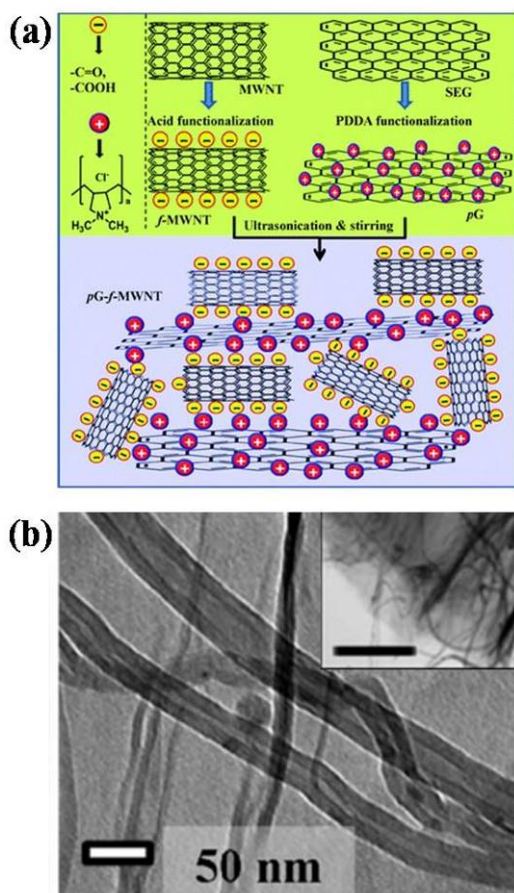


Figure 6. (a) Scheme of the graphene/MWNT nanocomposite synthesis and (b) HR-TEM image of G-CNT nanohybrids. Inset in panel b showed a large area of graphene/MWNT composite where wrapping of nanotubes between graphene sheets was visible. Scale bar

corresponds to 1 mm. Reprinted from ref. 25. Copyright 2012 The Royal Society of Chemistry.

To prepare G-CNTs nanohybrid aerogel a so-called green synthesis strategy was followed as pristine MWCNTs and GO were homogeneously dispersed with addition of dil. HCl containing vitamin C. Gelation formation was successfully controlled by adjusting pH. G-CNT gel was achieved under heat treatment and following supercritical  $\text{CO}_2$  drying that enabled the formation 3D aerogel structure of G-CNTs. The nanohybrids had high specific surface area of  $435 \text{ m}^2/\text{g}$ . Because of the interlinked nanostructures the hybrids exhibited excellent mechanical and electrical properties for example an electrical conductivity of  $7.5 \text{ Sm}^{-1}$  [26].

Lee et al. [27] synthesized vertically aligned CNTs on graphene sheets that were made on the copper foil by CVD method. Technically, arrays of aluminum and iron catalysts were deposited on the desired position by photolithography to grow the objects. Similarly, with CVD method and ethylene as carbon source Li et al. [28] grew vertically aligned CNTs (VACNTs) on  $3 \mu\text{m}$  thick graphene paper, which was loaded with iron nanoparticle catalyst. The grown efficiency of CNTs on the graphene paper was higher than the commercial substrate  $\text{Si}/\text{SiO}_2$ . It was found that the fast growth rate and prolonged catalyst lifetime on graphene substrate were also attributed to the favorable surface morphology and physical properties of the graphene paper. The large defects due to low temperature growth of VACNTs and

incomplete reduction of graphene were beneficially used for Li ion batteries and Solar cells. Because of the higher surface energy of exfoliated GO ( $62.1 \text{ mJ m}^{-2}$ ) than graphite ( $54.8 \text{ mJ m}^{-2}$ ) or graphene ( $46.7 \text{ mJ m}^{-2}$ ), Wei et al. [29] selected exfoliated GO as substrate to deposit catalyst nanoparticle for CNT growth and obtained G/CNT/G sandwich-like structure. Poor interaction of catalyst on the GO allowed the tip growth mechanism to grow CNTs. The 3D nanohybrid structure of G/CNT/G exhibited specific surface area of  $612 \text{ m}^2/\text{g}$ , much higher than that of graphene ( $202 \text{ m}^2/\text{g}$ ). Incorporation of CNTs between the graphene sheets acted as spacer to prevent them from aggregation and facilitate the rapid ion transport in the electrolyte surface.

Yang et al. [30] used poly(p-phenylenevinylene)(PPV) adhesion route to interconnect the graphene with CNTs to develop 3D N-doped reduced graphene oxide-PPV calcined-carbon nanotubes (N-RGO-PPV(c)-CNTs) nanohybrids. PPV precursor played like a "glue" for strong adhesion of the RGO and CNTs. Because PPV underwent transformation from the glassy state to a viscous state at high temperature, the N-RGO-PPV(c)-CNT composites with porous structure and ridge-like folded graphene flakes were formed during nitridation with thermal treatment. G/CNTs hybrids could be also synthesized by an electrostatic spray technique [31]. Acid functionalized GO and MWCNTs were prepared separately and could form a hybrid using an electrostatic spray. The introduction of MWCNTs into the GO network enhanced the elec-

tro-catalytic activity via mixed conductive network.

Recently, a novel multicomponent nanocarbon hybrids were prepared using acid-treated graphene and SWCNHs.  $\text{COOH}^-$  and  $\text{OH}^-$  functional groups on the nanocarbon surfaces led to hydrogen bond under hydrothermal treatment, which caused the nanohybrid formation. The nanohybrids exhibited ultra-micropores of 0.6 nm and mesopores of 2-12 nm with total pore volume  $0.2 \text{ cm}^3/\text{g}$  and specific surface area of  $210 \text{ m}^2/\text{g}$  (Figure 7). The specific surface area of the nanohybrids was higher than that of the pristine graphene and SWCNHs, indicating SWCNHs incorporation prevented the graphene nanosheets from aggregation. As shown in Figure 7b, SWCNHs were attached to the slightly wrinkled graphene nanosheets and prevented graphene from face-to-face stacking. On the other hand, the inter-connected graphene gave high conductivity to the hybrids. This novel nanostructures are favorable for electro-chemical application where charge transfer and mass transportations are necessary [32].

We recently investigated the effect of phosphoric acid activation on the nanoporous structures of carbon xerogels/carbon nanotubes (CX-CNTs) hybrids [33]. CXs loaded with nickel oxide were used as a substrate for the growth of CNTs with CVD method using camphor as a carbon precursor. In order to obtain large porosity, as-synthesized products were activated with phosphoric acid. CXs had a specific surface area of  $330 \text{ m}^2/\text{g}$ . Reasonably, after growing CNTs on the CXs the specific surface area of hybrids was significantly re-

duced to 95 m<sup>2</sup>/g. Nevertheless, after activation with phosphoric acid the specific surface area regained to 215 m<sup>2</sup>/g.

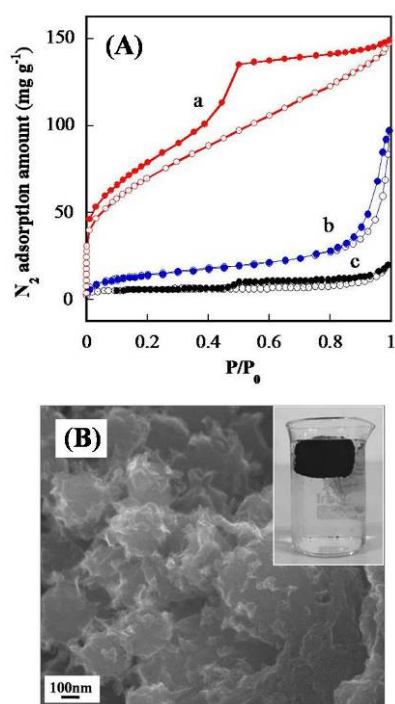


Figure 7. (A) Nitrogen adsorption (○)/desorption (●) isotherms on (a) G/SWCNHs, (b) SWCNHs and (c) GO at 77 K and (B) SEM image of the hybrids. Inset in panel B is the picture of G/SWCNHs in water. Reprinted from ref. 32. Copyright 2015 The Royal Society of Chemistry.

Xu et al. [34] developed a nanohybrids of CNTs/N-doped carbon polyhedral by dispersing CNTs in methanol with sonication, mixing them with Zn(NO<sub>3</sub>)<sub>2</sub>·6H<sub>2</sub>O and 2-methyl imidazole (2-MeIM) and final pyrolysis at 1000 °C for 4 h under N<sub>2</sub>. As shown in Figure 8, CNTs were inserted and intertwined with nitrogen-doped carbon polyhedra and remained size homogeneity and structural morphology of CNTs/ZIF-8. The nanohybrid exhibited high specific surface area of 898 m<sup>2</sup>/g, much higher than that of CNTs (149.1 m<sup>2</sup>/g). Pores might be

generated from the release of gases during the oxidation decomposition of organic linkers during the annealing process.

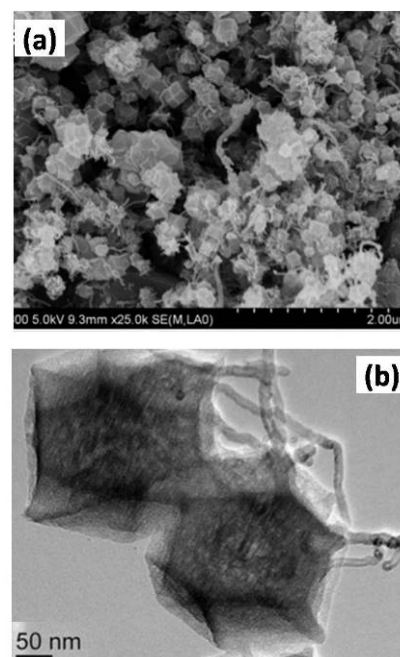


Figure 8. (a) SEM and (b) TEM images of CNTs/N-doped carbon polyhedral. Reprinted from ref. 34. Copyright 2016 Elsevier B.V.

### 2.3. Active materials loaded nanocarbon composites

The binding or loading of metals and metal component on nanocarbon surfaces can be achieved by means of post immobilization (ex-situ hybridization) or in-situ binding (in-situ crystallization). Post immobilization may suffer from low density and non-uniform coverage of nanostructures on the nanocarbon surfaces. In-situ method can not only grow crystalline nanostructures, but also reduce the nanocarbon from their oxidized form.

Yan et al. [35] loaded Ni on N-doped CNTs with a hydrothermal method. The hydrothermal treatment of MWCNTs and nickel salt at 150 °C in an aqueous solution containing ammonia and hydrazine led to

crystallization of the Ni nanoparticles, partial reduction of the oxidized CNTs and doping of nitrogen into the CNTs simultaneously.

Similarly, MWCNTs decorated with  $\text{CuCo}_2\text{S}_4$  nanoparticles were reported using acid-treated MWCNTs, metal salts dissolved in water,  $\text{Na}_2\text{CO}_3$  and triethylamine with hydrothermal treatment [36]. In that case, L-cysteine was used as sulfur source to convert the hydroxide into sulfide. Yamamoto et al. [37] prepared peptide (oligopeptide  $\beta$ -sheets **1**) based nanoparticle immobilization on graphene sheets. Thiol groups in the one end of peptide acted as binding agent and positively charged amino groups on the other end of peptide worked to bind the nanoparticles on graphene. The highly uniform immobilization of nanoparticles formed on the graphene as compared with no peptide linker (Figure 9).

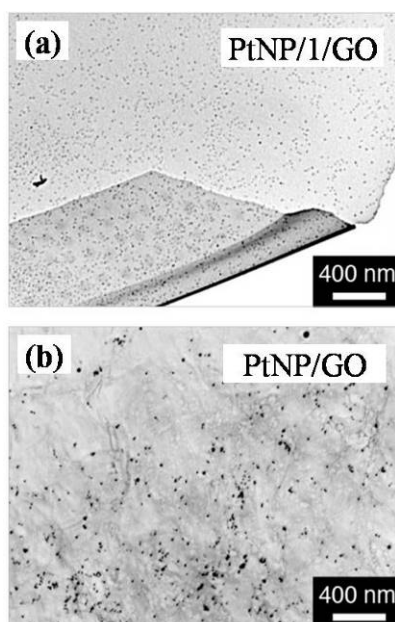


Figure 9. (a) TEM micrographs of PtNP/1/GO complex with peptide and (b) PtNP/GO composite without peptide. Reprinted from ref. 37. Copyright 2017 American Chemical Society.

Chen et al. [38] fabricated nanotubular hetero-structures of graphene–polypyrrole composites through a two-step CVD and electro-deposition method. Graphene was grown on nanoporous Ni-ligament. Then it underwent electrodeposition using three electrode system to achieve a polypyrrole composite. Ishihara et al. [39] made the hybrids of strongly coupled Ni-Fe nitrides on graphene by mixing Ni-Fe hydroxide (Ni:Fe = 3:1) and GO together and afterwards annealing treatment at  $700^\circ\text{C}$  under ammonia atmospheres. The electronic structure of the Ni-Fe nitride was modified by hybridizing with the N-doped graphene. The morphology of 2D  $\text{Ni}_3\text{FeN}$  nanoplates retained after annealing treatment due to the steric effect of N-doped graphene support.

Bando et al. [40] depicted the chemical etching of metal hydroxide through GO functional groups. Interaction between the basic hydroxide layers and the acidic groups of GO induced chemical etching of the hexagonal platelets, forming  $\beta\text{-Co}(\text{OH})_2$  hexagonal rings. Further annealing treatment converted them into  $\text{Co}_3\text{O}_4/\text{CoO}$ . Such selective etching and formation of metal hydroxide plates might be due to the H-bonding interactions between the hydroxyl planes of the platelets and the functional groups GO. Because of the highly defective structure, the dissolution started from central part of the hexagonal platelets rather than from outer region. The dissolution of the hydroxide platelets ceased when the  $\text{H}^+$  ions were exhausted, resulting the formation of rings. In comparison, there was no dissolution of

center part of hydroxide when graphite was used. It stated that the etching was caused by GO functional groups.

Ma et al. [41] reported  $\text{Fe}_9\text{S}_{10}$  nanocrystals anchored on N,S doped graphene. It was derived from the precursors of *p*-phenyl-bis(3,4-dicyanophenyl)thioether iron polyphthalocyanine (PTFePPc) and graphene. The PTFePPc with abundant N and S possessed highly conjugated  $\pi$ -electrons, thus it easily attached onto graphene *via* strong  $\pi$ - $\pi$  stacking interactions. Annealing the PTFePPc/G hybrids led to  $\text{Fe}_9\text{S}_{10}$  nanocrystals loaded on N,S doped graphene.

Recently authors developed copper-cobalt sulfide on the graphene nanosheets with a hydrothermal method. Nanobelt-like structure of metal sulfide possessed many defects and large surface roughness [42]. In another work, Ni-Co-S nanosheets was vertically grown on graphene with the diisopropylamine. The vertically oriented ultrathin porous  $\text{NiCo}_2\text{S}_4$  nanosheets avoided local aggregation as well as graphene stacking, thus resulting in a high BET surface area of  $111 \text{ m}^2/\text{g}$  in comparison with that of individual components [43]. Highly nanoporous hexagonal shell-plate  $\text{NiCo}_2\text{O}_4$  loaded on graphene was also prepared by us using triethylamine [44]. GO, metal salts and triethylamine were mixed together and underwent hydrothermal treatment to convert into metal hydroxide/G composite. Structural evolution was controlled by the inward contraction of Ni-Co system under slow annealing at  $300^\circ\text{C}$ . As shown in Figure 10, the samples were of smooth nanoplates before annealing. Continuous annealing caused the

evaporation of hydroxide ions and pore formation in the outer shells. Nanopore formation in the outer shells prevented the nanoplates from shell packing. The collapsed outer ring weakened the binding force between core and ring. Loosening of binding force and prostration of crystal packing were confirmed upon continuous annealing, which allowed the inner core to shrink inward and formed highly rigid structures.

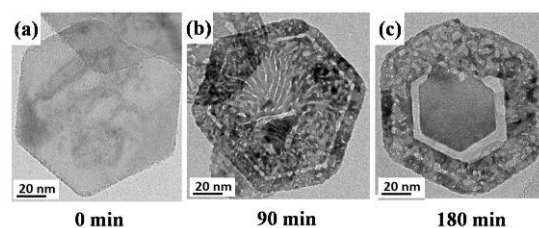


Figure 10. TEM images: (a) Before annealing, (b) Binding energy weakening at 90 min and (c) Inward shrinkage and the evaluation of gaps between core and shell at  $300^\circ\text{C}$ . Reprinted from ref. 44. Copyright 2017 WILEY-VCH Verlag GmbH & Co. KGaA, Weinheim.

### 3. Applications in electro-chemical energy storage

Because of global energy demands and increasing greenhouse gas, there is a vast interest in the energy storage technologies. Although renewable energy sources such as wind and solar energy output play important role in satisfying energy necessities, large gap between the supply and demands triggers -researchers to develop energy storage devices. It is estimated that world needs to double its energy by 2050 due to the increased human population and associated energy based appliance. Generally, the performance of energy device largely depends on the properties of the active electrode materials [45]. It is

demonstrated that functionalized nanocarbons enable the high performance of energy storage/conversion devices by their high conductivity, large specific surface area and excellent chemical stability [1-3, 46]. Moreover, based on their high mechanical stability and flexibility nanocarbon-based electrodes can be fabricated into the required shape and forms. Most recently, Liu et al. [47] designed flexible and robust sandwich-structured S-doped reduced graphene oxide/carbon nanotubes/polyaniline (S-rGO/CNTs/PANI) composite membranes as free-standing electrodes for supercapacitors. The flexible and free-standing electrode possessed good tensile strength of 6.53 MPa. S-rGO/CNTs/PANI exhibited maximum specific capacitance of 812 F/g at current density of 1 A/g and excellent cyclic stability. High feeding ratio of Na<sub>2</sub>S reduced the IR resistance *via* increasing the reduction degree of the GO nanosheets. The incorporated heteroatom and functional groups increased the wettability of electrodes. The superior performance could be attributed to the high specific surface area caused by CNTs, which created well-defined porous sandwiched structure. C-S-C species in the membrane electrodes could be oxidized to C-SO<sub>2</sub>-C and then reduced to C-S-C during the charge-discharge process, hence, the specific capacitance can be improved owing to such pseudo capacitive reaction of thiocarboxylic acid ester.

Lou et al. [48] grew CNTs onto graphene foam (GF) *via* catalytic chemical vapor deposition with the catalyst nanoparticles deposited onto GF by a hydrothermal method. By using the as-prepared 3D

GF/CNT hybrid films as current collectors, GF/CNT/MnO<sub>2</sub> hybrid film as the positive electrode and the GF/CNT/Ppy hybrid film as the negative electrode, flexible and lightweight asymmetric supercapacitors (ASCs) delivered an output voltage of 1.6 V and high energy/power density (22.8 W h kg<sup>-1</sup> at 860 W kg<sup>-1</sup> and 2.7 kW kg<sup>-1</sup> at 6.2 W h kg<sup>-1</sup>). Such ASCs demonstrated remarkable cycling stability of 90.2–83.5% after 10000 cycles.

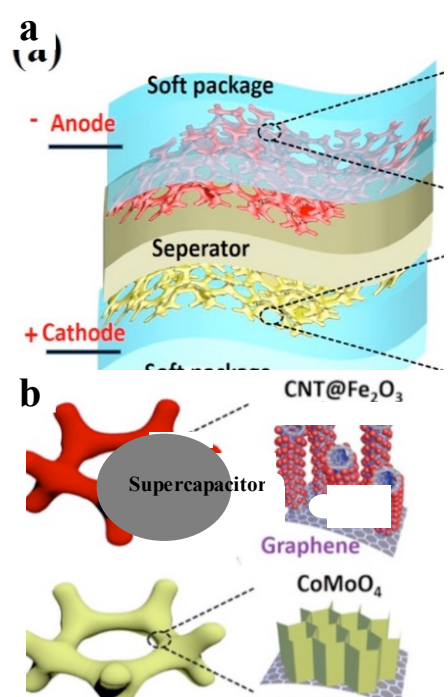


Figure 11. (a) Cycling ability with a current of 7 A/g and (b) Ragone plot of the GF–CNT@Fe<sub>2</sub>O<sub>3</sub>//GF–CoMoO<sub>4</sub> full cell. Reprinted from ref. 49. Copyright 2015 American Chemical Society.

Wang et al. [49] reported superior supercapacitor electrode of 3D hierarchical graphite foam–carbon nanotube framework coated iron oxide (GF–CNT@Fe<sub>2</sub>O<sub>3</sub>), in which Fe<sub>2</sub>O<sub>3</sub> was deposited with atomic layer deposition (ALD) method. Since the pseudo reaction took place predominately

on the surface as well as in the near-surface region of the metal oxides, after the  $\text{Fe}_2\text{O}_3$  coating, the areal capacitance was largely enhanced to  $\sim 470.5 \text{ mF/cm}^2$ , which was  $\sim 4$  times larger than that of GF-CNT ( $\sim 93.8 \text{ mF/cm}^2$ ). The full cell of anode based on this structure gave raised to a high energy of  $\sim 74.7 \text{ Wh/kg}$  at a power of  $\sim 1400 \text{ W/kg}$ , and  $\sim 95.4\%$  of the capacitance was retained after 50000 cycles (Figure 11).

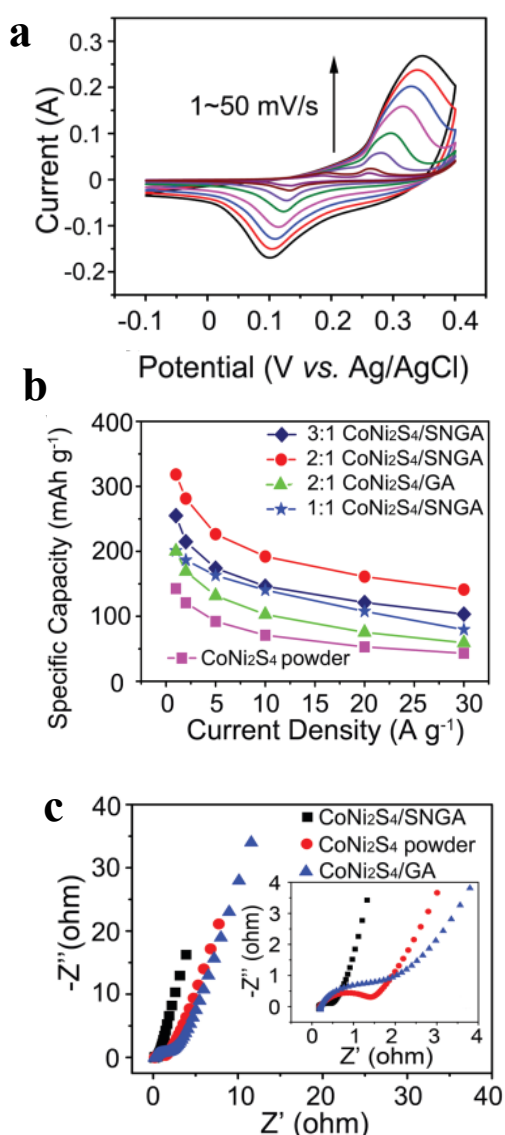


Figure 12. (a) CV curves of  $\text{CoNi}_2\text{S}_4/\text{SNGA}$  at the scan rate of  $1\text{--}50 \text{ mV s}^{-1}$ , (b) the comparison of specific discharge capacity for different ratios of  $\text{CoNi}_2\text{S}_4/\text{SNGA}$ ,  $\text{CoNi}_2\text{S}_4/\text{GA}$ , and  $\text{CoNi}_2\text{S}_4$  powder samples as a function of current

densities and (c) Nyquist curves of  $\text{CoNi}_2\text{S}_4/\text{SNGA}$ ,  $\text{CoNi}_2\text{S}_4/\text{GA}$ , and  $\text{CoNi}_2\text{S}_4$  electrodes. Inset in panel c shows high-frequency parts of the EIS spectra of the samples. Reprinted from ref. 50. Copyright 2016 The Authors. Published by WILEY-VCH Verlag GmbH & Co. KGaA, Weinheim.

Because the rate of reversible reaction at high current was largely limited by the poor conductivity of active materials, He et al. [50] synthesized a  $\text{CoNi}_2\text{S}_4$  loaded N,S doped graphene aerogel (SNGA) with the use of interconnected graphene to improved the conductivity of the electrode. As shown in Figure 12, the anodic and cathodic peaks shifted toward positive and negative potentials at the scan rate of  $1\text{--}50 \text{ mV s}^{-1}$ , respectively, suggesting the polarization of the electrode at a high scan rate. The rate capabilities of the materials remained ca.44% when the current density increased by 30 times, indicating the rich redox centers and the synergistic effect of both nickel and cobalt ions in the sulfides (redox reaction). N,S doped graphene loaded metal sulfides increased the whole network conductivity in comparison with non-doped composites. The asymmetric supercapacitor delivered a high volumetric power density of  $17.5 \text{ W cm}^{-3}$  and retained its high energy density of  $1.95 \text{ mWh cm}^{-3}$  at a current of  $1 \text{ mA}$ .

In order to maintain the rate capability, a core-shell nanostructure with  $\text{Ni-Co}_2\text{S}_4$  nanotube (NCS) as core and  $\text{Co}_x\text{Ni}_{(3-x)}\text{S}_2$  (CNS) nanosheets as a shell, was prepared using CVD grown 3D graphene layer on nickel foam (GNF) [51]. The

synergistic effects of graphene and metal sulfides showed enhanced specific capacitances with outstanding capacitance retention at high current densities and excellent cycling stability. The highest capacitance obtained for GNF/NCS/CNS core/shell structure is  $15.6 \text{ F/cm}^2$  at current density of  $10 \text{ mA/cm}^2$ . Even at high current density of  $100 \text{ mA/cm}^2$ , core/shell nanostructure still had high areal capacitance of  $11.6 \text{ F/cm}^2$ . As shown in Figure 13, a prototype asymmetric device was assembled with GNF/NCS/CNS core/shell as positive electrode and graphene as negative electrode. The novel structure showed excellent energy densities of  $29.9 \text{ Wh/kg}$  at  $15 \text{ mA}$ ; even at high power density of  $2460.6 \text{ W/kg}$  the energy density was still as very high as  $23.93 \text{ Wh/kg}$ . Such an ASC system was practical to light up the red LED light. We also explored vertically grown redox rich active materials on graphene sheets with a hydrothermal method. Prepared highly porous and exposed  $\text{Ni-Co}_2\text{S}_4/\text{G}$  nanocomposite delivered high capacitance of  $1498 \text{ F g}^{-1}$  at  $1 \text{ A g}^{-1}$  in  $1.0 \text{ M KOH}$  (Figure 14). With an increase in current density from  $1 \text{ A g}^{-1}$  to  $40 \text{ A g}^{-1}$ , the capacitance gradually decreased to  $1081 \text{ F g}^{-1}$ . The capacitance still maintained 72.3% even at the current density  $40 \text{ A g}^{-1}$ .

The incorporation of graphene and in-situ growth of active materials gives high electron conductivity, excellent reversibility and fast redox reactions. The high capacitive nanomaterial electrode coupled with graphene–single wall carbon nanohorn heterostructures provided a maximum energy of  $60.9 \text{ W h kg}^{-1}$  at  $1.4 \text{ kW kg}^{-1}$  power density [43].

This highly retained capacitance should be mainly ascribed to the exposed edge sites and porous heterostructures, which provided redox reactions, shorter electrolyte pathways and enhanced electrode–electrolyte contact. The interfacial contact between graphene and  $\text{Ni-Co}_2\text{S}_4$  increased the conductivity and surface roughness of the nanocomposite. It intensified the redox reactions, electrolyte ion interaction and diffusion rate on the electrode–electrolyte interface. ASC device was successfully used to rotate a motor, which demonstrated the promising application of this active materials.

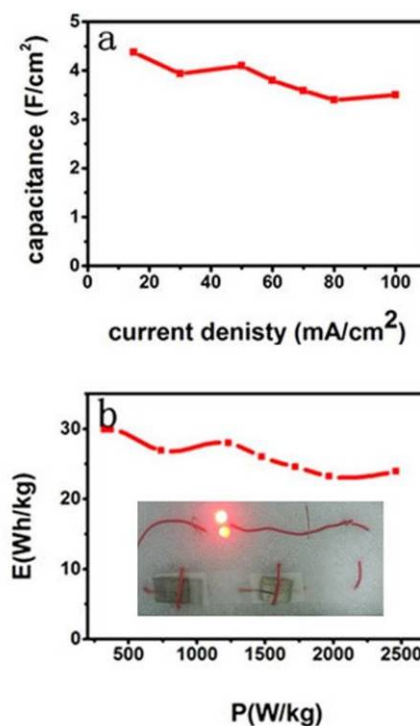


Figure 13. (a) Plot of areal capacitance as a function of current densities and (b) the Ragone plot of as synthesized electrode showing energy and power density relations. Inset in (b) shows two asymmetric supercapacitors connected in series and used to power on LEDs. Reprinted from ref. 51. Copyright 2017 The Authors.

Wang et al. [12] fabricated nitrogen and

oxygen dual-doped carbon nanohorn (N:CNH) *via* a facile arc-discharge. 9.9 pyridinic N and 39.3 at % pyrrolic N were successfully doped on SWCNHs surface *via* nitriding treatment. These two kinds of nitrogen dopants had the dominant contribution in the electrochemical capacitance for faradic pseudo capacitance. Their enhanced hydrophilic nature and large specific surface area were closely related to the high specific capacitance of  $240 \text{ F g}^{-1}$  at the current density of  $0.5 \text{ A g}^{-1}$  in  $1 \text{ M H}_2\text{SO}_4$  with three-electrode configuration.

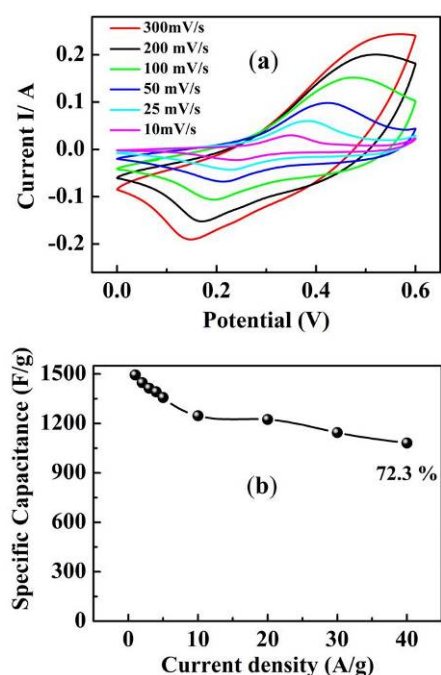


Figure 14. (a) Cyclic voltammetry curves from 10 to  $300 \text{ mV s}^{-1}$  and (b) specific capacitance vs. current density. Reprinted from ref. 43. Copyright 2017 The Royal Society of Chemistry.

Reviewing the recent progress in functionalized nanocarbons and their application in energy storage addressed a critical issue, that is further to improve the performance by optimizing the reaction conditions, pa-

rameters and fabrication processes in near future.

#### 4. Summary

Favorable synergistic effects of functionalized nanocarbons import new properties, large specific surface area and high conductivity, which lead the materials to be efficient in enhancing the performance for energy storage application. Different functionalization methods are known as incorporating heteroatoms or combining with active materials *via* chemical surface modification, physical mixing and in-situ formation, which offer ways to extend their applications in the field. Although vast opportunities remain for developing novel nanocarbon based materials, functionalization methods speed up their applications and will surely revolutionize the smart energy system in near future.

#### Acknowledgement

This work was supported by the National Natural Science Foundation of China (21273236) and supported from Science and Technology Planning Projects of Fujian Province of China (2015I0008) and Science and Technology Service Network Initiative (STS) Project of Fujian-CAS (2016T3036).

#### References

- (a) A. S. Aricò; P. Bruce; B. Scrosati; J.-M. Tarascon; W. van Schalkwijk, *Nat. Mater.* **2005**, *4*, 366; (b) D. R. Rolison; J. W. Long; J. C. Lytle; A. E. Fischer; C. P. Rhodes; T. M. McEvoy; M. E. Bourg; A. M. Lubers, *Chem. Soc. Rev.*, **2009**, *38* (1), 226-252; (c) L. Dai; D. W. Chang; J.-B. Baek; W. Lu, *Small* **2012**, *8* (8), 1130-1166; (d) D. N. Futaba; K.

- Hata; T. Yamada; T. Hiraoka; Y. Hayamizu; Y. Kakudate; O. Tanaike; H. Hatori; M. Yumura; S. Iijima, *Nat. Mater.*, **2006**, *5*, 987;(e) H. Nishihara; T. Kyotani, *Adv. Mater.*, **2012**, *24* (33), 4473-4498.
- 2) (a) Y. Tao; M. Endo; M. Inagaki; K. Kaneko, *J. Mater. Chem.*, **2011**, *21* (2), 313-323; (b) Y. Tao, M. Endo, K. Kaneko, in *Handbook of Innovative Nanomaterials: From Synthesis and Applications*, (Eds: Xiaosheng Fang & Limin Wu), Pan Stanford Publishing, 2012, 639-663; (c) K. C. Kemp; H. Seema; M. Saleh; N. H. Le; K. Mahesh; V. Chandra; K. S. Kim, *Nanoscale* **2013**, *5* (8), 3149-3171.
- 3) (a) C. J. Shearer; A. Cherevan; D. Eder, *Adv. Mater.* **2014**, *26* (15), 2295-2318; (b) H. Wang; H. Dai, *Chem. Soc. Rev.*, **2013**, *42* (7), 3088-3113; (c) Z.-S. Wu; G. Zhou; L.-C. Yin; W. Ren; F. Li; H.-M. Cheng, *Nano Energy* **2012**, *1* (1), 107-131; (d) H. Chang; H. Wu, *Energy Environ. Sci.*, **2013**, *6* (12), 3483-3507; (e) K. P. Annamalai, Y. Tao, in *Nanomaterials in Energy and Environmental Applications*, (Ed. J. He), Pan Stanford Publishing Pte. Ltd. 2016, 307-330.
- 4) (a) X. Wang; G. Sun; P. Routh; D.-H. Kim; W. Huang; P. Chen, *Chem. Soc. Rev.*, **2014**, *43* (20), 7067-7098; (b) T. Asefa; X. Huang, *Chemistry – A European Journal* **2017**, *23* (45), 10703-10713; (c) I. S. Amiin; Z. Pu; X. Liu; K. A. Owusu; H. G. R. Monestel; F. O. Boakye; H. Zhang; S. Mu, *Adv. Funct. Mater.*, **2017**, *27*, 1702300.
- 5) S. Yasuda; A. Furuya; Y. Uchibori; J. Kim; K. Murakoshi, *Adv. Funct. Mater.*, **2016**, *26* (5), 738-744.
- 6) K. Qu; Y. Zheng; Y. Jiao; X. Zhang; S. Dai; S.-Z. Qiao, *Adv. Energy Mater.*, **2017**, *7* (9), 1602068.
- 7) H. Huang; J. Zhu; W. Zhang; C. S. Tiwary; J. Zhang; X. Zhang; Q. Jiang; H. He; Y. Wu; W. Huang; P. M. Ajayan; Q. Yan, *Chem. Mater.*, **2016**, *28* (6), 1737-1745.
- 8) Y. Ito; Y. Shen; D. Hojo; Y. Itagaki; T. Fujita; L. Chen; T. Aida; Z. Tang; T. Adschiri; M. Chen, *Adv. Mater.*, **2016**, *28* (48), 10644-10651.
- 9) R. Yuge; M. Yudasaka; K. Toyama; T. Yamaguchi; S. Iijima; T. Manako, *Carbon* **2012**, *50* (5), 1925-1933.
- 10) R. Yuge; S. Bandow; M. Yudasaka; K. Toyama; S. Iijima; T. Manako, *Carbon* **2017**, *111*, 675-680.
- 11) X. Wu; L. Cui; P. Tang; Z. Hu; D. Ma; Z. Shi, *Chem. Comm.*, **2016**, *52* (31), 5391-5393.
- 12) X. Wang; M. Lou; X. Yuan; W. Dong; C. Dong; H. Bi; F. Huang, *Carbon* **2017**, *118*, 511-516.
- 13) (a) V. Georgakilas; J. N. Tiwari; K. C. Kemp; J. A. Perman; A. B. Bourlinos; K. S. Kim; R. Zboril, *Chem. Rev.*, **2016**, *116* (9), 5464-5519; (b) V. Georgakilas; M. Otyepka; A. B. Bourlinos; V. Chandra; N. Kim; K. C. Kemp; P. Hobza; R. Zboril; K. S. Kim, *Chem. Rev.*, **2012**, *112* (11), 6156-6214.
- 14) J. L. Bahr; J. Yang; D. V. Kosynkin; M. J. Bronikowski; R. E. Smalley; J. M. Tour, *J. Am. Chem. Soc.*, **2001**, *123* (27), 6536-6542.
- 15) Q. Yang; X. Pan; K. Clarke; K. Li, *Ind. Eng. Chem. Re.* **2012**, *51* (1), 310-317.
- 16) D. Voiry; G. Pagona; E. D. Canto; L. Ortolani; V. Morandi; L. Noe; M. Monthieux; N. Tagmatarchis; A. Penicaud, *Chem. Comm.*, **2015**, *51* (24), 5017-5019.
- 17) G. Pagona; N. Tagmatarchis; J. Fan; M. Yudasaka; S. Iijima, *Chem. Mater.*, **2006**, *18* (17), 3918-3920.
- 18) Y.-L. Zhao; J. F. Stoddart, *Acc. Chem. Research* **2009**, *42* (8), 1161-1171; (b) S. Utsumi, M. Kanamaru, H. Honda, H. Kanoh, H. Tanaka, T. Ohkubo, H. Sakai, M. Abe, K. Kaneko, *J. Colloid Interf. Sci.* **2007**, *308*, 276-284.
- 19) A. Di Crescenzo; V. Ettore; A. Fontana, *Beilstein J. Nanotech.* **2014**, *5*, 1675-1690.
- 20) J. Chen; C. P. Collier, *J. Phys. Chem. B* **2005**, *109*(16), 7605-7609.
- 21) D. Yu; L. Dai, *J. Phys. Chem. Lett.*, **2010**, *1* (2), 467-470.

- 22) Y. Wang; Y. Wu; Y. Huang; F. Zhang; X. Yang; Y. Ma; Y. Chen, *J. Phys. Chem. C* **2011**,115 (46), 23192-23197.
- 23) A. Izadi-Najafabadi; T. Yamada; D. N. Futaba; M. Yudasaka; H. Takagi; H. Hatori; S. Iijima; K. Hata, *ACS Nano* **2011**,5 (2), 811-819.
- 24) Q. Zheng; B. Zhang; X. Lin; X. Shen; N. Yousefi; Z.-D. Huang; Z. Li; J.-K. Kim, *J. Mater. Chem* **2012**,22 (48), 25072-25082.
- 25) B. P. Vinayan; R. Nagar; V. Raman; N. Rajalakshmi; K. S. Dhathathreyan; S. Ramaprabhu, *J. Mater. Chem.* **2012**,22 (19), 9949-9956.
- 26) Z. Sui; Q. Meng; X. Zhang; R. Ma; B. Cao, *J. Mater. Chem.*,**2012**,22 (18), 8767-8771.
- 27) U. J. Kim; I. L. H. Lee; J. J. Bae; S. Lee; G. H. Han; S. J. Chae; F. Güneş; J. H. Choi; C. W. Baik; S. I. Kim; J. M. Kim; Y. H. Lee, *Adv. Mater.*,**2011**,23 (33), 3809-3814.
- 28) S. Li; Y. Luo; W. Lv; W. Yu; S. Wu; P. Hou; Q. Yang; Q. Meng; C. Liu; H.-M. Cheng, *Adv. Energy Mater.*,**2011**,1 (4), 486-490.
- 29) Z. Fan; J. Yan; L. Zhi; Q. Zhang; T. Wei; J. Feng; M. Zhang; W. Qian; F. Wei, *Adv. Mater.*,**2010**,22 (33), 3723-3728.
- 30) Y. Fu; C. Tian; F. Liu; L. Wang; H. Yan; B. Yang, *Nano Res.*, **2016**,9 (11), 3364-3376.
- 31) P. Han; Y. Yue; Z. Liu; W. Xu; L. Zhang; H. Xu; S. Dong; G. Cui, *Energy Environ. Sci.*,**2011**,4 (11), 4710-4717.
- 32) K. P. Annamalai; J. Gao; L. Liu; J. Mei; W. Lau; Y. Tao, *J. Mater. Chem. A* **2015**,3 (22), 11740-11744.
- 33) (a) N. A. Fathy; K. P. Annamalai; Y. Tao, *Adsorption* **2017**,23 (2), 355-360; (b) K.P. Annamalai, N. A. Fathy, Y. Tao, *J. Sol-Gel Sci. Tech.*, **2017**(84), 515 – 521
- 34) X. Xu; M. Wang; Y. Liu; Y. Li; T. Lu; L. Pan, *Energy Storage Materials* **2016**,5, 132-138.
- 35) Z. Zhuang; S. A. Giles; J. Zheng; G. R. Jenness; S. Caratzoulas; D. G. Vlachos; Y. Yan, *Nature Communications* **2016**,7, 10141.
- 36) M. Zhang; K. P. Annamalai; L. Liu; T. Chen; J. Gao; Y. Tao, *RSC Adv.*,**2017**,7 (34), 20724-20731.
- 37) T. Mizutaru; G. Marzun; S. Kohsakowski; S. Barcikowski; D. Hong; H. Kotani; T. Kojima; T. Kondo; J. Nakamura; Y. Yamamoto, *ACS Applied Materials & Interfaces* **2017**,9 (11), 9996-10002.
- 38) H. Kashani; L. Chen; Y. Ito; J. Han; A. Hirata; M. Chen, *Nano Energy* **2016**,19, 391-400.
- 39) Y. Fan; S. Ida; A. Staykov; T. Akbay; H. Hagiwara; J. Matsuda; K. Kaneko; T. Ishihara, *Small* **2017**,13 (25), 1700099.
- 40) C. Nethravathi; C. R. Rajamathi; M. Rajamathi; X. Wang; U. K. Gautam; D. Golberg; Y. Bando, *ACS Nano* **2014**,8 (3), 2755-2765.
- 41) X.-X. Ma; Y. Su; X.-Q. He, *Catalysis Science & Technology* **2017**,7 (5), 1181-1192.
- 42) L. Liu; K. P. Annamalai; Y. Tao, *New Carbon Materials* **2016**,31 (3), 336-342.
- 43) K. P. Annamalai; L. Liu; Y. Tao, *J. Mater. Chem. A* **2017**,5 (20), 9991-9997.
- 44) K. P. Annamalai; L. Liu; Y. Tao, *Adv. Mater. Interf.*,**2017**,4 (16), 1700219.
- 45) P. Simon; Y. Gogotsi, *Nat. Mater.***2008**,7, 845.
- 46) Q. Zhang; E. Uchaker; S. L. Candelaria; G. Cao, *Chem. Soc. Rev.*,**2013**,42 (7), 3127-3171.
- 47) D. Liu; P. Du; W. Wei; H. Wang; Q. Wang; P. Liu, *Electrochimica Acta* **2017**,233 (Supplement C), 201-209.
- 48) J. Liu; L. Zhang; H. B. Wu; J. Lin; Z. Shen; X. W. Lou, *Energy & Environ. Sci.*, **2014**,7 (11), 3709-3719.
- 49) C. Guan; J. Liu; Y. Wang; L. Mao; Z. Fan; Z. Shen; H. Zhang; J. Wang, *ACS Nano* **2015**,9 (5), 5198-5207.
- 50) G. He; M. Qiao; W. Li; Y. Lu; T. Zhao; R. Zou; B. Li; J. A. Darr; J. Hu; M.-M. Titirici; I. P. Parkin, *Adv. Sci.*,**2017**,4 (1), 1600214.
- 51) L. G. Beka; X. Li; W. Liu, *Sci. Rep.*,**2017**,7 (1), 2105.